SCIENCE CHINA
Information Sciences

• RESEARCH PAPER •

August 2016, Vol. 59 082307:1–082307:16
doi: 10.1007/s11432-015-5446-z

High-precision deformation monitoring algorithm for GBSAR system: rail determination phase error compensation

Cheng HU, Mao ZHU, Tao ZENG*, Weiming TIAN & Cong MAO

Beijing Key Laboratory of Embedded Real-time Information Processing Technology, Beijing Institute of Technology, Beijing 100081*, China*

Received June 4, 2015; accepted July 17, 2015; published online February 17, 2016

Abstract In recent years, the repeat-pass GBSAR (ground based synthetic aperture radar) system has demonstrated its capacity to acquire deformation. Nevertheless, in a variety of applications, it needs to measure the deformation with the precision up to 0.1 mm, which could not be reached by utilizing the traditional PS (permanent scatterer) algorithm in most cases. Generally, one of the main reasons could be summarized into the phase error caused by the rail determination error, because the precision of rail determination might degrade during long working hours. However, the traditional PS algorithm could not compensate for the phase error caused by the rail determination error. In order to solve the problems, we modify the conventional PS algorithm. Firstly, we deduced the transformation relationship between the rail determination error and its corresponding interferometric phase error. Then, the phase errors caused by the atmosphere and the rail determination error were jointly compensated. The experimental data, which were obtained in Fangshan District in Beijing (China), were used to test and verify the performance of the new algorithm. After the comparison between the results processed by the new algorithm and those processed by the traditional algorithm, the proposed method demonstrated its ability to obtain high-precision deformation.

Keywords permanent scatterer (PS), synthetic aperture radar (SAR), ground-based SAR, deformation monitoring, radar

Citation Hu C, Zhu M, Zeng T, et al. High-precision deformation monitoring algorithm for GBSAR system: rail determination phase error compensation. Sci China Inf Sci, 2016, 59(8): 082307, doi: 10.1007/s11432-015-5446-z

1 Introduction

In recent years, the repeat-pass GBSAR (ground based synthetic aperture radar) technology has gained an increasing interest as a deformation monitoring tool [1–10]. With regard to the repeat-pass GBSAR system, it is capable to monitor deformation in all-weather condition. As a non-contact measurement, it is advantaged by high safety factor of measurements. In terms of technical features, because of the zero-baseline configuration, it does not need an external DEM to remove the topographic phase as spaceborne DInSAR (differential SAR interferometry) does [11, 12]. Furthermore, it is featured by relatively high time sampling rate, which could acquire the deformation of the scenario at the frequency of 5–10 min.

* Corresponding author (email: zengtao@bit.edu.cn)

In this paper, it focuses on taking advantage of the PS (permanent scatterer) algorithm to obtain high-precision deformation information of scenarios from the data acquired by repeat-pass GBSAR system. PS algorithm was proposed by Ferretti et al. from Politecnico di Milano in Italy, and was initially used for the spaceborne differential interferometry processing [13–15]. It has successfully solved the problems caused by temporal and geometric decorrelation in the traditional differential interferometry processing. Meanwhile, a great deal of research institutions have made a lot of researches on GBSAR deformation measurements, especially the University of Florence [16,17] and IDS (Ingegneria Dei Sistemi) Corporation. The IBIS-L system developed by them has been widely applied in many fields. Besides, Spanish UPC (Universitat Polit cnica de Catalunya) University [18], and Germany Technical University of Darmstadt (Technische Universitat Darmstadt) [19,20], etc., have also made great contributions to the development of GBSAR deformation monitoring technology. In 2012, China's Beijing Institute of Technology started to carry out the research on deformation measurement by using the GBSAR system. They independently developed the GBSAR system, and had used it to carry out the deformation measurement experiments.

Currently, a number of fields need to acquire the deformation measurement information with the precision up to 0.1 mm. However, for high-precision deformation measurement demands, the processing results of GBSAR data by using the traditional PS algorithm are difficult to meet the requirements. One of the main reasons stems from the rail determination error. In the course of long-term monitoring, the rail determination precision of the sliding rail may degrade. Therefore, the rail determination error will introduce the additional deformation error.

In order to solve the problems brought about by the rail determination error, modifications are proposed in this paper on the basis of the traditional PS algorithm. We firstly deduced the transforming relationship between the rail determination error and its corresponding interferometric phase error. Then, we jointly estimated and compensated for the atmospheric phase and the phase error induced by the rail determination error through the LS (least square) method. Ultimately, the high-precision deformation was obtained.

The rest of this paper is organized as follows. Section 2 will focus on the description of GBSAR system, the fundamental principle of GBSAR deformation measurement technology and the existing problems of the traditional PS algorithm. In Section 3, the phase error of SAR image introduced by the rail determination error is presented. In Section 4, the transforming relationship between the rail determination error and its corresponding interferometric phase error is deduced. Then, the method to jointly compensate for the atmospheric phase and the rail determination phase error is elaborated. At last, the remained phase error after just using the atmospheric model to compensate the phase error is analyzed. In Section 5, the measured data processing results are presented and analyzed. Finally, the conclusion is presented in Section 6.

2 The description of GBSAR system and the principle of GBSAR deformation measurement

The picture of the GBSAR radar sensor designed and developed by the Beijing Institute of Technology is shown in Figure 1. The system is able to monitor mm-level deformation both in terms of short-range or long-range. The radar system is operating in the Ku-band, while its transmitting and receiving devices share the same antenna. In the process of the deformation measurement, the radar sensor is placed on a precision sliding rail with the length of 2.4 m. It could collect SAR echo data at the shortest frequency of 5–10 min.

In contrast to the spaceborne differential interferometric processing, the biggest advantage of the ground-based SAR differential interferometry is that the radar system could be placed on a precision sliding rail in order to achieve the zero baseline configuration. It eventually leads to the easier processing of deformation generation. In the course of actual measurement, the basic parameters of the GBSAR system are shown in Table 1.

The basic theory for repeat-pass GBSAR system to monitor deformation could be described as follows.

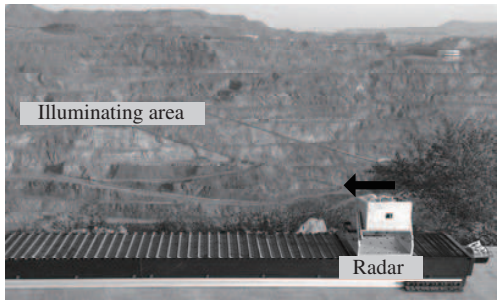

Figure 1 The picture of GBSAR system.

Table 1 The basic parameters of the system

Parameters	Value	Parameters	Value
Central frequency	16.02 GHz	Bandwidth	320 MHz
Linear scanning length	2.4 m	Illuminating distance	50–2000 m
Range resolution	0.48 m	Azimuth resolution	4 m@1 km

Before the occurrence of deformation, the distance between the target point and the radar is R_1. Then, after the SAR imaging process, the phase of the target point can be expressed as

$$\varphi_1 = -\frac{4\pi}{\lambda} R_1 + \varphi_{\text{atm1}} + \varphi_{\text{noise1}}, \tag{1}$$

where φ_{atm1} and φ_{noise1} denote the atmospheric phase and noise phase at the illumination time before the occurrence of deformation, respectively.

At a certain instant, deformation takes place, and the value of deformation in the LOS (line-of-sight) direction is Δd. After the occurrence of deformation, the distance from the target to the radar is R_2. Then, after the SAR imaging processes, the phase of the target point can be expressed as

$$\varphi_2 = -\frac{4\pi}{\lambda} R_2 + \varphi_{\text{atm2}} + \varphi_{\text{noise2}}, \tag{2}$$

where φ_{atm2} and φ_{noise2} denote the atmospheric phase and noise phase at the illumination time after the occurrence of deformation, respectively. After the interferometric processing, the target's interferometric phase can be expressed as

$$\phi = \varphi_2 - \varphi_1 = -\frac{4\pi}{\lambda} (R_2 - R_1) + (\varphi_{\text{atm2}} - \varphi_{\text{atm1}}) + (\varphi_{\text{noise2}} - \varphi_{\text{noise1}}). \tag{3}$$

In the ideal case, we assume that the atmospheric phase during those two irradiation processes is identical, i.e., $\varphi_{\text{atm1}} = \varphi_{\text{atm2}}$, and the noise phase during those two irradiation processes is 0, i.e., $\varphi_{\text{noise1}} = \varphi_{\text{noise2}} = 0$. Concurrently, if the repeat-pass characteristics of the rail is superior during those two illumination processes and the complete zero baseline configuration is realized, then $R_2 - R_1 = \Delta d$. Therefore, Eq. (3) can be simplified as

$$\Delta d = -\frac{\lambda}{4\pi} \phi. \tag{4}$$

Eq. (4) establishes the relationship between the deformation and interferometric phase of the target point. Thus, in the ideal case, it is able to obtain information about the deformation of the target point by calculating the interferometric phase.

However, in reality, the atmospheric parameters vary with time, which results in the fact that the atmospheric phase corresponding to different time is disparate. Meanwhile, in the long-term measurement, due to the effect of temporal decorrelation, the scattering properties of numerous targets will change. In addition, the thermal noise will also change with time when the radar works for long hours, which leads to the fact that the noise phase will change in the observation process. Finally, although the repeat-pass GBSAR system uses the sophisticated sliding rail, it may also be subject to rail determination error in

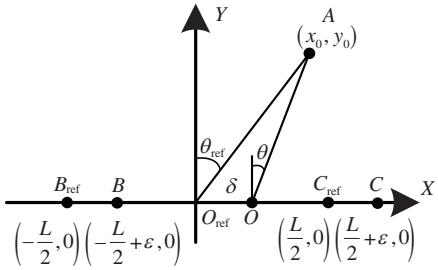

Figure 2 The model of rail determination error.

the long working process. In the presence of the rail determination error, a new deformation error will be introduced. It can be expressed as follows by a mathematical formula:

$$R_2 - R_1 = \Delta d + \Delta d_{\text{rail}}, \tag{5}$$

where Δd_{rail} denotes the deformation error caused by the rail determination error.

As a result, the changes of the three components (the atmospheric phase, the noise phase and the rail determination error) will all reduce the precision of deformation measurements for the repeat-pass GBSAR. In the case of the presence of these errors, the interferometric phase of the target point can be written as

$$\phi = -\frac{4\pi}{\lambda}\Delta d + \Delta\varphi_{\text{atm}} + \Delta\varphi_{\text{rail}} + \Delta\varphi_{\text{noise}}, \tag{6}$$

where $\Delta\varphi_{\text{atm}}$ denotes the changes of the atmospheric phase during two observation processes, $\Delta\varphi_{\text{rail}}$ signifies the phase introduced by the rail determination error during two observation processes, and $\Delta\varphi_{\text{noise}}$ represents the other phase error components, respectively.

For the PS point, $\Delta\varphi_{\text{noise}}$ is relatively low. Therefore, we would neglect its influence. Generally, in the conventional PS algorithm, only the atmospheric phase model was established and applied to compensate for the atmospheric phase. Nevertheless, other phase error components, such as the rail determination phase error, were not modeled and then could not be compensated effectively. Finally, these uncompensated phase error components would lead to the degradation of the deformation precision in the whole image. Therefore, the traditional PS algorithm could not realize high-precision deformation measurement.

In order to achieve high-precision deformation measurement in the presence of these errors, thus, in this paper, we modified the PS algorithm based on the existing PS algorithm for the GBSAR system. According to the rail determination phase error model, we deduced the transformation relationship between the rail determination error and the deformation error. Then, both the atmospheric phase model and rail determination error model were applied to accurately compensate for the errors introduced by the atmospheric phase and the rail determination error with the LS method. Ultimately, the high-precision deformation measurement could be realized.

3 The phase error of SAR image induced by the rail determination error

Based on the basic information of the precise sliding rail, the rail determination error could be modeled as the repositioning error. As shown in Figure 2, the radar sensor moves along X-axis, and the length of the rail is L. In the nominal case, the radar sensor would move from B_{ref} to C_{ref}, and the center of the nominal synthetic aperture is O_{ref}. Nevertheless, in a certain pass, as the presence of the rail determination error, the radar sensor moves from B to C, and the center of the real synthetic aperture is O. We assume the rail determination error is δ, which means the lengths of three lines ($B_{\text{ref}}B$, $O_{\text{ref}}O$ and $C_{\text{ref}}C$) are δ. For a certain target $A(x_0, y_0)$, the nominal azimuth angle is θ_{ref}, and the real azimuth angle in the observation is θ.

At a certain instant in one pass, the radar sensor's coordinate is $(x+\delta, 0)$, and $x \in \left[-\frac{L}{2}, \frac{L}{2}\right]$. As the result, the distance from the target point A to the radar sensor at the instant could be expressed as

$$R = \sqrt{(x+\delta-x_0)^2 + y_0^2}. \tag{7}$$

Then, the Taylor's expansion of (7) at $x=0$ could be written as

$$R(x) = R(0) + R'(0)\,x + \frac{R''(0)}{2!}x^2 + \cdots, \tag{8}$$

where

$$\begin{aligned} R(0) &= \sqrt{(\delta-x_0)^2 + y_0^2}, \\ R'(0) &= \frac{\delta - x_0}{\sqrt{(\delta-x_0)^2 + y_0^2}} = -\sin\theta, \\ R''(0) &= \frac{y_0^2}{\left[(\delta-x_0)^2 + y_0^2\right]^{\frac{3}{2}}} = \frac{\cos^2\theta}{R(0)}. \end{aligned} \tag{9}$$

The returned signal $S(x)$ from the target point A to the antenna in any instant after pulse compression could be expressed by

$$s(x) = \exp\left(-\mathrm{j}\frac{4\pi}{\lambda}R(x)\right) = \exp\left(-\mathrm{j}\frac{4\pi}{\lambda}\left(R(0) - (\sin\theta)\,x + \frac{\cos^2\theta}{2R(0)}x^2 + \cdots\right)\right). \tag{10}$$

Generally, it is difficult to analyze the phase of the target after azimuth compression theoretically in a closed form. Therefore, we introduce the deramp-FFT algorithm in a closed form to evaluate the performance of focusing algorithm and the phase of the target in the presence of the rail determination error.

SAR focusing can be performed by multiplying the received signal with a deramp function followed by Fourier transformation in azimuth direction,

$$g(\kappa|x_0, y_0) = \int_{-\frac{L}{2}}^{\frac{L}{2}} s(x)\,h^{-1}(x)\exp(-\mathrm{j}2\pi x\kappa)\,\mathrm{d}x. \tag{11}$$

The deramp function is chosen to include the terms higher and equal to the second order of (10) based on the nominal position of the radar sensor, which is presented as in the following:

$$h^{-1}(x) = \exp\left(\mathrm{j}\frac{4\pi}{\lambda}\left(\frac{\cos^2\theta_{\mathrm{ref}}}{2R_{\mathrm{ref}}(0)}x^2 + \cdots\right)\right), \tag{12}$$

where

$$R_{\mathrm{ref}}(0) = \sqrt{x_0^2 + y_0^2}. \tag{13}$$

So that the integrand in (11) is reduced to the following form (ignoring higher order terms):

$$g(\kappa) = \int_{-\frac{L}{2}}^{\frac{L}{2}} \exp\left(-\mathrm{j}\frac{4\pi}{\lambda}\left[R(0) - (\sin\theta)\,x + \frac{\cos^2\theta}{2R(0)}x^2 - \frac{\cos^2\theta_{\mathrm{ref}}}{2R_{\mathrm{ref}}(0)}x^2\right]\right)\exp(-\mathrm{j}2\pi\kappa x)\mathrm{d}x. \tag{14}$$

With the approximation $\theta \approx \theta_{\mathrm{ref}}$ and $R_{\mathrm{ref}}(0) - R(0) \approx \delta\sin\theta$, Eq. (14) could be written as

$$g(\kappa) = \exp\left(-\mathrm{j}\frac{4\pi}{\lambda}R(0)\right)\int_{-\frac{L}{2}}^{\frac{L}{2}} \exp\left(-\mathrm{j}2\pi\left(-\frac{2}{\lambda}\sin\theta + \kappa\right)x\right)\exp\left(-\mathrm{j}\frac{2\pi}{\lambda}\cos^2\theta\frac{\delta\sin\theta}{R_{\mathrm{ref}}(0)\,R(0)}x^2\right)\mathrm{d}x. \tag{15}$$

Here, we would analyze the second order term of the integrand, which is defined as follows:

$$\varphi_{2\mathrm{nd}} = \frac{2\pi}{\lambda}\cos^2\theta\frac{\delta\sin\theta}{R_{\mathrm{ref}}(0)\,R(0)}x^2. \tag{16}$$

Table 2 The parameters for the second order phase term analysis

Parameters	Symbol	Value
Central frequency	f	16.02 GHz
Azimuth angle	θ	$-45°$– $45°$
Target range	$R(0)$	1 km
Rail determination error	δ	0.2 mm
Rail length	L	2 m

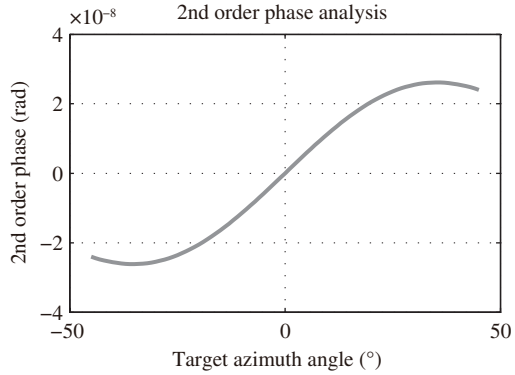

Figure 3 Variation of the second order term as a function of the azimuth angle.

The values of the parameters, which are used to analyze the second order term, are listed in Table 2. Figure 3 shows the second order term varies with the azimuth angle. We could see that the second order term would be the maximum value when the azimuth angle is about 35°. However, the maximum value of the second order term is still in the order of 10^{-8} rad. Therefore, we could neglect its influence.

After neglecting the second order term, Eq. (15) could be expressed as

$$g(\kappa) = \exp\left(-\mathrm{j}\frac{4\pi}{\lambda}R(0)\right)\int_{-\frac{L}{2}}^{\frac{L}{2}}\exp\left(-\mathrm{j}2\pi\left(-\frac{2}{\lambda}\sin\theta+\kappa\right)x\right)\mathrm{d}x. \tag{17}$$

After the integration, Eq. (17) could be written as

$$g(\kappa) = L\mathrm{sinc}\left[\pi L\left(\kappa-\frac{2}{\lambda}\sin\theta\right)\right]\exp\left(-\mathrm{j}\frac{4\pi}{\lambda}R(0)\right). \tag{18}$$

The focused image has the maximum amplitude in κ-space at

$$\kappa_0 = \frac{2}{\lambda}\sin\theta = \frac{2}{\lambda}\frac{x_0}{R(0)} = \frac{2}{\lambda}\frac{x_0}{\sqrt{x_0^2+y_0^2}}. \tag{19}$$

The phase value of the target A in the focused image is $\varphi = \frac{4\pi}{\lambda}R(0)$, which is a measure of the range from the real synthetic aperture center O to the target A, enabling its use for SAR interferometry.

4 Modeling and joint compensation of rail determination phase error and atmospheric phase

In general, for most of the target points, the rail determination phase error and the atmospheric phase are probably greater than the phase caused by the deformation. As a consequence, if we could not compensate for the rail determination phase error and the atmospheric phase effectively, the GBSAR system is difficult to acquire the high-precision deformation information.

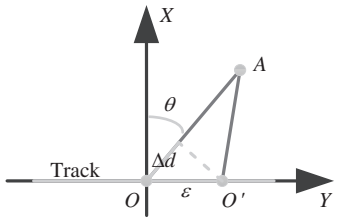

Figure 4 The schematic diagram of the rail determination phase error theory.

4.1 Rail determination phase error modeling

Ideally, the precise sliding rail can realize complete repeat-pass to meet zero-baseline requirements. Nonetheless, in the process of long-term measurement, due to a variety of reasons, the precision of rail determination might degrade, resulting in the incomplete repeat-pass of the radar during the motion process. After the imaging process, it may lead to the changes between the synthetic aperture centers of the different passes.

As illustrated in Figure 4, due to the impact of rail determination error, the synthetic aperture center point O in the 1st pass shifted to the point O' in the 2nd pass. The distance ε between these two points was defined as the repeat-pass error. Generally, if the rail determination error $\delta \sim N\left(0, \sigma^2\right)$, the repeat-pass error $\varepsilon \sim N\left(0, 2\sigma^2\right)$. The azimuth angle corresponding to the target point in the scenario was θ. In accordance with the fundamental theory of the ground-based SAR, with regard to the SAR data in the 1st pass, the phase of the target point A in the 1st image could be expressed as

$$\varphi_{A,1} = -\frac{4\pi}{\lambda} R_{OA}. \tag{20}$$

In a similar way, in the 2nd pass SAR image, the phase corresponding to the target point A can be expressed as

$$\varphi_{A,2} = -\frac{4\pi}{\lambda} R_{O'A}. \tag{21}$$

Although the target point was not subject to deformation between the two observation processes, the shift of the synthetic aperture center also gave rise to the change in the slant range. Thus, it introduced additional interferometric phase, which could be expressed by the mathematical formula as follows:

$$\Delta\varphi_{\text{rail}} = -\frac{4\pi}{\lambda}\left(R_{OA} - R_{O'A}\right). \tag{22}$$

Meanwhile, in general, the repeat-pass error ε was in the scale of sub-mm, namely $R_{OA} \gg \varepsilon$. Therefore, the relationship between the slant range shift Δd and its corresponding repeat-pass error ε could be expressed as

$$\Delta d = R_{OA} - R_{O'A} = \varepsilon \sin\theta. \tag{23}$$

Then, Eq. (22) could be further simplified as

$$\Delta\varphi_{\text{rail}} = -\frac{4\pi}{\lambda}\varepsilon \sin\theta. \tag{24}$$

It was revealed from (24) that, the phase error introduced by the rail determination error was associated with the target's azimuth angle, and was independent of the target's slant range. If the repeat-pass error ε was 0.2 mm, then it would bring about 0.1 mm deformation error for the target with the azimuth angle of 30°.

4.2 Atmospheric phase modeling

Due to the influence of atmosphere, the propagation velocity of the electromagnetic wave in troposphere will be reduced, which will lead to the propagation delay relative to the theoretical value. Meanwhile,

owing to the variation in the atmospheric conditions at different times, the propagation velocity of the electromagnetic wave at different times will vary and then lead to the disparity in the propagation delay. The disparity in the propagation delay at different times is the reason why the atmospheric phase is generated in the interferometric data [21, 22].

Since the observation scenario of GBSAR is relatively small, its scope is generally within a few Km. Thus, for an observation, the atmosphere is homogeneous in the scenario, in other words, the atmospheric refraction index is invariant in the entire scenario for one observation. In this case, when the atmospheric parameters change between two observation times, the atmospheric phase component of the interferometric phase can be expressed as [16]

$$\Delta\varphi_{\mathrm{ATM},n}(t) = 10^{-6}\frac{4\pi f_{\mathrm{c}} R_n}{\mathrm{c}}\Delta N(t), \tag{25}$$

where f_{c} is the central frequency, c is the speed of light, R_n means the nth target's slant range and $\Delta N(t)$ represents the variation of the atmospheric refraction index during two observation times.

Based on (25), it is indicated that, in the conditions of invariable atmospheric refraction index in one observation, the atmospheric phase component changes linearly with the slant range.

4.3 Interferometric phase model for stationary PS

In practice, taking into account both the rail determination phase error and the atmospheric phase, if no deformation occurs at a certain PS during two observation times, the interferometric phase of this PS can be represented as follows:

$$\Delta\varphi = Ar + B + C\sin\theta + e, \tag{26}$$

where the parameters to be estimated consist of A, B and C. Specifically, r and θ denote the slant range and azimuth angle corresponding to the target point, respectively. Generally, every pixel's slant range r and azimuth angle θ could be calculated precisely based on SAR image information. Meanwhile, we could find that, $Ar + B$ is the atmospheric phase, $C\sin\theta$ is the phase caused by the rail determination error, and e signifies the un-modelled phase error, respectively.

By considering the stationary PSs within the interested scenario, their interferometric phase $\Delta\varphi_1$, $\Delta\varphi_2$, ..., $\Delta\varphi_k$, ..., $\Delta\varphi_n$ can be written as

$$\begin{cases} \Delta\varphi_1 = Ar_1 + B + C\sin\theta_1 + e_1, \\ \Delta\varphi_2 = Ar_2 + B + C\sin\theta_2 + e_2, \\ \quad\cdots \\ \Delta\varphi_k = Ar_k + B + C\sin\theta_k + e_k, \\ \quad\cdots \\ \Delta\varphi_n = Ar_n + B + C\sin\theta_n + e_n. \end{cases} \tag{27}$$

Eq. (27) could be expressed in a matrix mode as follows:

$$\Delta\Phi = X\beta + E, \tag{28}$$

where

$$\Delta\Phi = \begin{bmatrix} \Delta\varphi_1 \\ \Delta\varphi_2 \\ \vdots \\ \Delta\varphi_n \end{bmatrix} X = \begin{bmatrix} r_1, 1, \sin\theta_1 \\ r_2, 1, \sin\theta_2 \\ \vdots \\ r_n, 1, \sin\theta_n \end{bmatrix} \beta = \begin{bmatrix} A \\ B \\ C \end{bmatrix} E = \begin{bmatrix} e_1 \\ e_2 \\ \vdots \\ e_n \end{bmatrix}, \tag{29}$$

where X is a matrix of $n \times 3$, which contains the location information for each PS. $\Delta\Phi$ and E are the vectors of $n \times 1$, which contain the interferometric phase information and the random noise phase error information for each PS. β is the vector of 3×1, which contains the three parameters to be estimated in each interferogram.

4.4 Analysis of phase error after the compensation only using the atmospheric phase model

If both the atmospheric phase and the rail determination phase error exist, Eq. (27) could express the interferometric phase of the PS, which is stationary during two observations. Here, we rewrite the equation in another form

$$\Delta\Phi = X_1\beta_1 + X_2\beta_2 + E, \tag{30}$$

where

$$X_1 = \begin{bmatrix} r_1,1 \\ r_2,1 \\ \vdots \\ r_n,1 \end{bmatrix} \beta_1 = \begin{bmatrix} A \\ B \end{bmatrix} X_2 = \begin{bmatrix} \sin\theta_1 \\ \sin\theta_2 \\ \vdots \\ \sin\theta_n \end{bmatrix} \beta_2 = [C]\,. \tag{31}$$

In the process of phase error compensation, we only consider the atmospheric phase model. Then, the estimated parameters could be expressed as

$$\hat{\beta}_1 = \left(X_1^{\mathrm{T}}X_1\right)^{-1}X_1^{\mathrm{T}}\Delta\Phi. \tag{32}$$

Thus, the estimated atmospheric phase could be written as

$$\Delta\hat{\Phi}_{\mathrm{Atm}} = X_1\hat{\beta}_1. \tag{33}$$

As the result, the remaining phase error after the atmospheric phase compensation is

$$\begin{aligned}
\Delta &= \Phi - \hat{\Phi}_{\mathrm{Atm}} = (I - X_1\left(X_1{}^{\mathrm{T}}X_1\right)^{-1}X_1{}^{\mathrm{T}})\Phi = (I - X_1\left(X_1{}^{\mathrm{T}}X_1\right)^{-1}X_1{}^{\mathrm{T}})\left(X_1\beta_1 + X_2\beta_2 + E\right) \\
&= X_1\beta_1 + X_2\beta_2 + E - X_1\left(X_1{}^{\mathrm{T}}X_1\right)^{-1}X_1{}^{\mathrm{T}}X_1\beta_1 - X_1\left(X_1{}^{\mathrm{T}}X_1\right)^{-1}X_1{}^{\mathrm{T}}X_2\beta_2 - X_1\left(X_1{}^{\mathrm{T}}X_1\right)^{-1}X_1{}^{\mathrm{T}}E \\
&= X_1\beta_1 - X_1\left(X_1{}^{\mathrm{T}}X_1\right)^{-1}\left(X_1{}^{\mathrm{T}}X_1\right)\beta_1 + (I - X_1\left(X_1{}^{\mathrm{T}}X_1\right)^{-1}X_1{}^{\mathrm{T}})X_2\beta_2 + (I - X_1\left(X_1{}^{\mathrm{T}}X_1\right)^{-1}X_1{}^{\mathrm{T}})E \\
&= X_2\beta_2 - X_1\left(X_1{}^{\mathrm{T}}X_1\right)^{-1}X_1{}^{\mathrm{T}}X_2\beta_2 + E - X_1\left(X_1{}^{\mathrm{T}}X_1\right)^{-1}X_1{}^{\mathrm{T}}E \\
&= \Phi_{\mathrm{rail}} - \Phi_{\mathrm{railpro}} + E - \Phi_{\mathrm{Epro}},
\end{aligned} \tag{34}$$

where $\Phi_{\mathrm{rail}} = X_2\beta_2$ means the rail determination phase error vector. Meanwhile, based on the theory of LS (least square) estimation, the $n \times n$ matrix $X_1\left(X_1{}^{\mathrm{T}}X_1\right)^{-1}X_1{}^{\mathrm{T}}$ is known as the orthogonal projection matrix. $\Phi_{\mathrm{railpro}} = X_1\left(X_1{}^{\mathrm{T}}X_1\right)^{-1}X_1{}^{\mathrm{T}}X_2\beta_2$ and $\Phi_{\mathrm{Epro}} = X_1\left(X_1{}^{\mathrm{T}}X_1\right)^{-1}X_1{}^{\mathrm{T}}E$ are the projections of the rail determination error vector and phase noise vector onto the atmospheric phase subspace respectively.

As could be seen in (34), there are four terms remaining as phase errors. Φ_{rail} and E are the rail determination phase error vector and the noise phase vector, respectively. Here, we would use the simulation method to analyze the other two projection phase terms (Φ_{railpro} and Φ_{Epro}). Generally, we assume the azimuth angle θ is uniformly distributed between $-45°$ and $45°$. The slant range r and the noise phase e are supposed to be gauss distributed, which could be described as $r \sim N\left(1000\ \mathrm{m}, 300^2\ \mathrm{m}^2\right)$ and $e \sim N\left(0, 0.2^2\ \mathrm{rad}^2\right)$. $C = \frac{4\pi}{\lambda}\varepsilon$ sets as 0.136, when the central frequency is 16.2 GHz and the repeat-pass error ε is 0.2 mm. Finally, a total of 10000 points are used in the simulation.

In the simulation, we define the rail determination phase error projection ratio vector R_{rail} and the noise phase projection ratio vector R_E as

$$\begin{aligned}
R_{\mathrm{rail}}(n) &= \Phi_{\mathrm{railpro}}(n)/\Phi_{\mathrm{rail}}(n), \\
R_E(n) &= \Phi_{\mathrm{Epro}}(n)/E(n).
\end{aligned} \tag{35}$$

Figure 5 shows the distribution of the two ratio vector R_{rail} and R_E. Based on the statistic data, we could see that 90% points' rail determination phase error projection ratio and 89% points' noise phase projection ratio are less than 0.05. Therefore, we could neglect the influence of the two projection phase terms (Φ_{railpro} and Φ_{Epro}).

Consequently, if we just use the atmospheric phase model to compensate the phase error, the rail determination phase error Φ_{rail} and the noise phase E are the main factors to cause deformation error. In another words, the rail determination phase error Φ_{rail} could not be compensated when only using the atmospheric phase model in the compensation process.

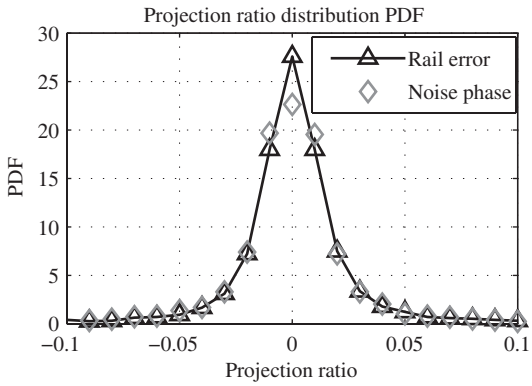

Figure 5 Rail determination phase error and noise phase projection ratio distribution.

4.5 Joint estimation and compensation of rail determination phase error and atmospheric phase

If both the atmospheric phase model and the rail determination phase error model are considered, then, the estimation of the rail determination phase error and the atmospheric phase can be transformed into the estimation of the three parameters (A, B and C). According to the least square estimation theory, the parameter vector β can be written as

$$\beta = \left(X^{\mathrm{T}}X\right)^{-1}X^{\mathrm{T}}\Delta\Phi. \tag{36}$$

Thus, the sum of the estimated atmospheric phase and the estimated rail determination phase error can be expressed as

$$\Delta\hat{\Phi}_{\mathrm{Est}} = X\hat{\beta}, \tag{37}$$

where $\Delta\hat{\Phi}_{\mathrm{Est}}$ is the vector of $n \times 1$, which contains the sum of the estimated atmospheric phase and the estimated rail determination phase error corresponding to each PS point. Then, the remaining phase error after the joint compensation of rail determination phase error and atmospheric phase is

$$\begin{aligned}\Delta' &= \Phi - \hat{\Phi}_{\mathrm{Est}} = \left(I - X\left(X^{\mathrm{T}}X\right)^{-1}X^{\mathrm{T}}\right)\Phi = \left(I - X\left(X^{\mathrm{T}}X\right)^{-1}X^{\mathrm{T}}\right)(X\beta + E)\\ &= X\beta + E - X\left(X^{\mathrm{T}}X\right)^{-1}X^{\mathrm{T}}X\beta - X\left(X^{\mathrm{T}}X\right)^{-1}X^{\mathrm{T}}E\\ &= X\beta - X\left(X^{\mathrm{T}}X\right)^{-1}\left(X^{\mathrm{T}}X\right)\beta + \left(I - X\left(X^{\mathrm{T}}X\right)^{-1}X^{\mathrm{T}}\right)E\\ &= E - X\left(X^{\mathrm{T}}X\right)^{-1}X^{\mathrm{T}}E.\end{aligned} \tag{38}$$

Comparing (38) with (34), we could conclude that the rail determination phase error has been completely compensated after using the rail determination phase error model.

In the process, we could utilize the iterative process to precisely compensate the phase error. Firstly, the difference between the real interferometric phase $\Delta\Phi$ and the sum of the estimated atmospheric phase and the estimated rail determination phase error $\Delta\hat{\Phi}_{\mathrm{Est}}$ for each PS point embodies the matching degree of the phase model in (26) against the phase information of this PS, which is designated to characterize whether this PS is stationary. Then, the selected stationary PSs are prepared for the next estimation, so as to obtain the more precise estimation. The stationary judgment of a certain PS point can be fulfilled as follows:

$$\left|\Delta\Phi - \Delta\hat{\Phi}_{\mathrm{Est}}\right| < \varphi_{\mathrm{Threshold}}. \tag{39}$$

The iterative process is terminated until all of the remaining points are in conformity with the conditions of (39). If the atmospheric phase and the rail determination phase error can be well compensated, the precision of deformation generation can be improved to a great extent.

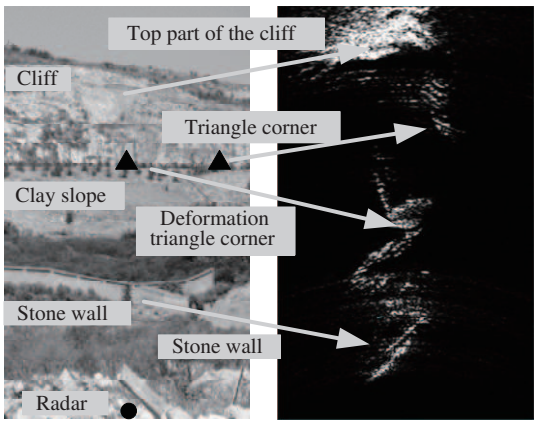

Figure 6 The scenario photo and SAR image of Fangshan District, Beijing.

Table 3 The basic parameters of the experiment

Parameters	Value	Parameters	Value
Starting time	2013.10.16 10:30	Ending time	2013.10.16 17:30
Number of image	40	Sample rate	10 min
Range limit	230–700 m	Azimuth limit	−120 m– +120 m
Range resolution	0.48 m	Azimuth resolution	2 m@500 m
PS ADI threshold	0.15	Number of PSs	19769

5 Real data processing results

5.1 Experimental introduction

Figure 6 shows the optical picture of the observation scenario. The target of observation refers to a quarry in Beijing's Fangshan District. The distinct targets in the scenario consist of cliffs, clay slopes and stone wall. On October 16, 2013, seven hours of continuous observations were carried out on the quarry and a total of 40 SAR images were collected. During the experiment, two corner reflectors were emplaced in the scenario, which were 472 m and 563 m away from the radar respectively. Taking into account that the observation period was not long, we assumed the displacements were zero in the whole scenario. As a result, in order to simulate the deformation occurred in the scenario, the corner reflector with 472 m away from the radar was mounted on a deformation regulator, while the precision of the deformation regulator was up to 0.01 mm.

The basic parameters of the experiment are summarized in Table 3. Because the observation scenario was small, the variation of atmospheric phase was not particularly dramatic. Therefore, it was not difficult to conduct phase unwrapping. Also, it should be noted that there were relatively dense trees between the stone wall and the clay slope in the observation scenario, which resulted in the significant impact of temporal decorrelation. Meanwhile, according to the basic information of the sliding rail, the corresponding rail determination precision was 0.2 mm. As a result, in some interferograms, we could clearly see the influence caused by the sliding rail determination error.

5.2 Description of experimental results

Figure 7 shows the deformation generation results from the interferometric data, which were obtained between two acquisitions separated roughly 20 min in time, by using different phase error models for compensation. Figure 7(a) is the results after compensation by only using the linear atmospheric model. It is evident that the deformation values in the scenario vary with the azimuth angle. As the temporal baseline of the interferometric data was merely 20 min, it was believed that there was no deformation occurring in the scenario during this period of time. Accordingly, the generated deformation was considered

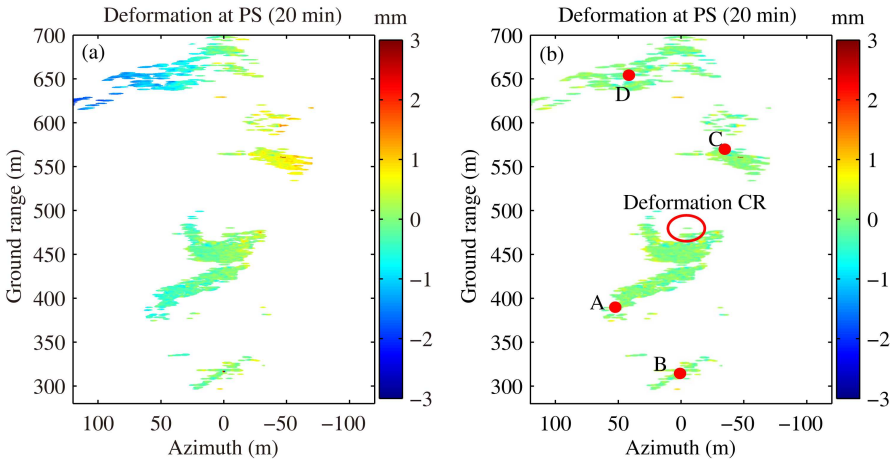

Figure 7 The deformation generation results by using different phase compensation models. (a) Only using the linear atmospheric model; (b) simultaneously using the linear atmospheric model and the rail determination phase error model.

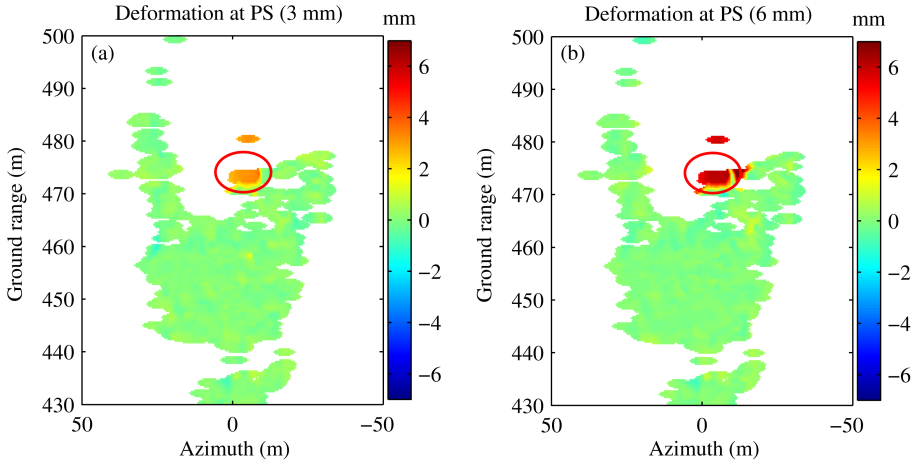

Figure 8 The deformation generation results of PSs in Fangshan District and the displacement of the corner reflector. (a) 3 mm; (b) 6 mm.

to be other errors. Figure 7(b) shows the results after the compensation by using the linear atmospheric model and the rail determination phase error model simultaneously. We could see that no significant deformation existed in the entire scenario, which was consistent with the assumption. Therefore, we could conclude that the rail determination error exerted an influence on the final deformation. It should adopt the model proposed in this paper to compensate for the rail determination phase error.

5.3 Precision analysis of deformation

5.3.1 *Analysis of deformation generation for the scenarios*

Since the experimental period was only 7 h, it was possible that no significant deformation occurred in the scenario during the observation. Thus, in the experimental process, we used the deformation regulator to precisely adjust the displacement of the deformation corner reflector (the adjustment precision of the displacement was 0.01 mm) to simulate the deformation occurring in the scenario. In the process of deformation generation, the linear atmospheric model and the rail determination phase error model were applied to jointly compensate for the phase error. Figure 8 shows the accumulative deformation generation results of the scenario when the deformation corner reflector adjusted different deformation quantities (3 mm and 6 mm). It was revealed from the deformation results that, with the increase in the adjustment of the deformation corner reflector, there was significant deformation information appearing in the deformation corner reflector region. The positive displacement meant the occurrence

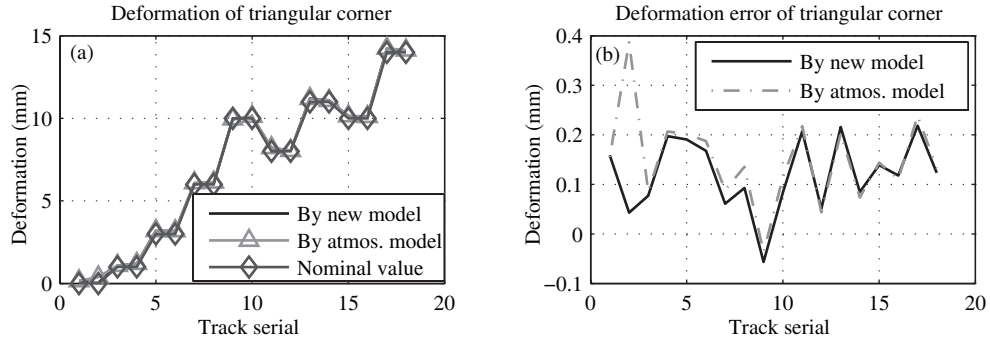

Figure 9 (a) The deformation generation results of the deformation corner reflector; (b) the deformation generation error results of the deformation corner reflector.

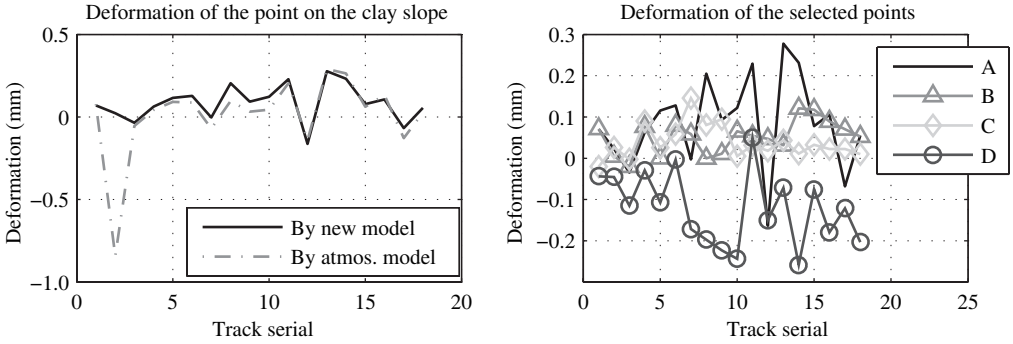

Figure 10 (a) The deformation generation results of the natural target point A; (b) LOS displacements with time observed at four representative points.

of deformation toward the radar, which was also consistent with the actual adjustment direction of deformation. Meanwhile, for other regions within the scenario, there was no significant deformation in the results. This was also in conformity with the assumption that there would be no significant deformation in the scenario during the relatively short observation time.

5.3.2 *Precision analysis of deformation generation for specific target points*

Figure 9 shows the time-series deformation obtained at the deformation corner reflector after compensating for the phase error by only using the atmospheric phase model, and jointly using the atmospheric phase model and the rail determination phase error model, respectively. As indicated in Figure 9(a) and (b), except for the generated deformation at the 2nd rail, the deformation results obtained by using those two compensation methods were substantially identical. When compared with the nominal deformation, both methods could obtain high-precision deformation results. However, for the 2nd rail data, it might correspond to a larger rail determination error. By comparing the results of the two compensation methods, it was clear that the error was reduced from 0.39 mm to 0.05 mm in case of jointly using the atmospheric phase model and the rail determination phase error model for phase error compensation. It also suggested that, when the rail determination error was large, the rail determination error would have a greater impact on the deformation generation results, thus it needed to apply the rail determination phase error model to compensate for the phase error.

Figure 10(a) shows the time-series generated deformation at point A in Figure 7(b). As assuming that no deformation occurred at the point A in the whole observation process, the generated deformation at the point A could be considered as the deformation generation error. Identical with the case at the deformation corner reflector, in case of only using the linear atmospheric phase model for compensation, the 2nd rail data was subject to greater residual deformation error. Meanwhile, it was worth noting that for the 2nd rail data, the deformation error at point A reached 0.8 mm, which was greater than the deformation error at the deformation corner reflector. It could be attributed to the fact that the azimuth

Table 4 The statistical results of the time-series deformation generation error deviation of the deformation corner reflector and the natural target point A

Phase compensation method	Deformation corner reflector (mm)	Point A (mm)
Only using the linear atmospheric model	0.0914	0.2434
Simultaneously using two models	0.0736	0.1115

Table 5 The statistical results of the time-series deformation generation error deviation of the four selected points

Point	Slant range (m)	Deformation error (mm)
A	407	0.1115
B	323	0.0867
C	563	0.0870
D	662	0.1530

angle of point A was greater than that of the deformation corner reflector. Consequently, the impact caused by the rail determination error would be greater.

In order to analyze the deformation generation precision of a certain target point by using different methods, the time-series deformation error deviation was used to assess their performance. The mathematical expression for the time-series deformation error deviation of a target point is defined as follows:

$$\sigma_{\text{temporal}} = \sqrt{\frac{\sum_{i=1}^{K} \left(d_{i,\text{gen}} - d_{i,\text{nom}}\right)^2}{K-1}}, \tag{40}$$

where K denotes the number of interferograms, i denotes the ordinal number of the interferogram, $d_{i,\text{gen}}$ represents the generated deformation of this point in the ith interferogram, and $d_{i,\text{nom}}$ signifies the nominal deformation of this point in the ith interferogram, respectively. In respect of the deformation corner reflector, the nominal deformation was the adjusted deformation. With respect to the natural target point A, the nominal deformation was zero upon assuming that no deformation occurred at the target point during the observation period.

Table 4 shows the statistical results of the time-series deformation error deviation of the deformation corner reflector and the natural target point A by using those two phase error compensation methods. Both for the deformation corner reflector and the natural target point A, if adopting the compensation method considering the rail determination phase error model, the deformation precisions have been improved and basically reached the deformation precision level of 0.1 mm. Thereby, it achieved high-precision GBSAR deformation monitoring.

Finally, we selected four natural points on the scenario to analyze their deformation history. The phase compensation model applied to generate deformation was the joint use of the linear atmospheric model and the rail determination error model. In Figure 10(b), the LOS (line of sight) displacements of the four pixels highlighted in Figure 7(b) were plotted together. The four natural points were corresponding to different targets respectively (A: clay slope, B: stone wall, C: stable corner reflector, D: cliff).

Table 5 shows the statistical results of the time-series deformation error deviation of the four points. By analyzing the three natural targets (A, B and D), we could conclude that the longer the slant range was, the lower the deformation precision was. It could be attributed to the fact that the intensities of the closer targets would be stronger. However, the deformation precision of the target C was higher than that of the target A, while the slant range of the target C was longer to the radar. This was because the target C was the corner reflector and its intensity was stronger than other natural targets.

6 Conclusion

With respect to the GBSAR system, its survey scope can range from tens of meters to several kilometers, and it can observe the target at the shortest frequency of 5 min. In addition, its range resolution and azimuth resolution can be up to 0.5 m and 2 m@500 m, respectively. As the GBSAR system has these features, it has wonderful application prospects in the slope hazard monitoring.

In order to further enhance the performance of GBSAR, it requires the GBSAR system to provide 0.1 mm-level high precision deformation. Nonetheless, in case of applying the traditional deformation generation algorithm, it is hard to achieve such high precision. One of the main problems is the rail determination error. In the long working hours, the rail determination precision of the sliding rail might degrade, and then it would introduce the deformation error. To address the issue, the paper has deduced the transforming relationship between the repeat-pass error and its corresponding interferometric phase error. Furthermore, the rail determination phase error and the atmospheric phase are jointly compensated by the LS method. Ultimately, it has accomplished the high-precision deformation measurement.

In practice, we used both the new algorithm and the traditional algorithm to process the measured data acquired in Fangshan District in Beijing (China) respectively. By analyzing the results, especially for the data characterized by greater rail determination error between two rails, we could conclude that the new algorithm could accurately compensate for the deformation error components caused by the rail determination error. The analysis of the deformation generation results on the deformation corner reflector and the natural target demonstrated that, the deformation precision could reach the level of 0.1 mm. The results had completely validated that the new algorithm had the ability to obtain high-precision deformation information.

Acknowledgements This work was supported by National Natural Science Foundation of China (Grant Nos. 61120106004, 61225005, 61471038 and 61427802), Chang Jiang Scholars Program (Grant No. T2012122), and 111 Project of China (Grant No. B14010).

Conflict of interest The authors declare that they have no conflict of interest.

References

1 Tarchi D, Rudolf H, Pieraccini M, et al. Remote monitoring of buildings using a ground-based SAR: application to cultural heritage survey. Inter Remote Sens, 2000, 21: 3545–3551
2 Monserrat O, Crosetto M, Luzi G. A review of ground-based SAR interferometry for deformation measurement. ISPRS J Photogramm Remote Sens, 2014, 93: 40–48
3 Caduff R, Schlunegger F, Kos A, et al. A review of terrestrial radar interferometry for measuring surface change in the geosciences. Earth Surface Process Landforms, 2015, 40: 208–228
4 Luzi G, Pieraccini M, Mecatti D, et al. Ground-based radar interferometry for landslides monitoring: Atmospheric and instrumental decorrelation sources on experimental data. IEEE Trans Geosci Remote Sens, 2004, 42: 2454–2466
5 Aguasca A, Broquetas J, Mallorqui J, et al. A solid state L to X-band flexible ground-based SAR system for continuous monitoring applications. In: Proceedings of the IEEE IGARSS, Anchorage, 2004. 757–760
6 Tarchi D, Casagli N, Fanti R, et al. Landslide monitoring by using ground-based SAR interferometry: an example of application to the Tessina landslide in Italy. Eng Geol, 2003, 68: 15–30
7 Leva D, Nico G, Tarchi D, et al. Temporal analysis of a landslide by means of a ground-based SAR interferometer. IEEE Trans Geosci Remote Sens, 2003, 41: 745–752
8 Antonello G, Tarchi D, Casagli N, et al. SAR interferometry from satellite and ground-based system for monitoring deformations on the Stromboli volcano. In: Proceedings of the IEEE IGARSS, Anchorage, 2004. 633–636
9 Pieraccini M, Casagli N, Luzi G, et al. Landslide monitoring by ground-based radar interferometry: a field test in Valdarno (Italy). Inter Remote Sens, 2003, 24: 1385–1391
10 Pieraccini M, Luzi G, Mecatti D, et al. Ground-based SAR for short and long term monitoring of unstable slopes. In: Proceedings of the 3rd European Radar Conference, EuRAD, Manchester, 2006. 92–95
11 Wang Q, Huang H, Dong Z, et al. High-precision, fast DEM reconstruction method for spaceborne InSAR. Sci China Inf Sci, 2011, 54: 2400–2410
12 Zeng T, Zhang T, Tian W, et al. A novel subsidence monitoring technique based on space-surface bistatic differential interferometry using GNSS as transmitters. Sci China Inf Sci, 2015, 58: 062304(16)
13 Ferretti A, Prati C, Rocca F. Non-uniform motion monitoring using the permanent scatterers technique. In: Proceedings of 2nd Int. Workshop ERS SAR Interferometry, FRINGE, Liège, 1999. 1–6
14 Ferretti A, Prati C, Rocca F. Nonlinear subsidence rate estimation using permanent scatterers in differential SAR interferometry. IEEE Trans Geosci Remote Sens, 2000, 38: 2202–2212
15 Ferretti A, Prati C, Rocca F. Permanent scatterers in SAR interferometry. IEEE Trans Geosci Remote Sens, 2001, 39: 8–20
16 Noferini L, Takayama T, Pieraccini M, et al. Analysis of ground-based SAR data with diverse temporal baselines. IEEE Trans Geosci Remote Sens, 2008, 46: 1614–1623
17 Noferini L, Pieraccin M, Mecatti D, et al. Permanent scatterers analysis for atmospheric correction in ground-based SAR interferometry. IEEE Trans Geosci Remote Sens, 2005, 43: 1459–1471

18 Iglesias R, Fabregas X, Aguasca A, et al. Atmospheric phase screen compensation in ground-based SAR with a multiple-regression model over mountainous regions. IEEE Trans Geosci Remote Sens, 2014, 52: 2436–2449
19 Rodelsperger S, Becker M, Gerstenecker C, et al. Digital elevation model with the ground-based SAR IBIS-L as basis for volcanic deformation monitoring. J Geodynamics, 2010, 49: 241–246
20 Rodelsperger S, Laufer G, Gerstenecker C, et al. Monitoring of displacements with ground-based microwave interferometry: IBIS-S and IBIS-L. J Appl Geodesy, 2010, 4: 41–54
21 Pipia L, Fabregas X, Aguasca A, et al. Atmospheric artifact compensation in ground-based DInSAR applications. IEEE Geosci Remote Sens Lett, 2008, 5: 88–92
22 Iannini L, Guarnieri A M. Atmospheric phase screen in ground-based radar: statistics and compensation. IEEE Geosci Remote Sens Lett, 2011, 8: 537–541